ADVANCED MATERIALS

Supporting Information

for *Adv. Mater.*, DOI: 10.1002/adma.201703024

Harnessing Photochemical Shrinkage in Direct Laser Writing for Shape Morphing of Polymer Sheets

*Anton A. Bauhofer, Sebastian Krödel, Jan Rys, Osama R. Bilal, Andrei Constantinescu, and Chiara Daraio**

Supporting Information

Harnessing Photochemical Shrinkage in Direct Laser Writing for Shape Morphing of Polymer Sheets

*Anton A. Bauhofer, Sebastian Krödel, Jan Rys, Osama, R. Bilal, Andrei Constantinescu, Chiara Daraio**

Analytical Modeling

Supporting Table S1. Nomenclature

Variable	Explanation
E	Young's Modulus of the photopolymer
g	Gravitational acceleration
I_i	Moment of inertia of single layers
l_{crit}	Critical length after which delamination occurs
M_i	Representative bending moment
n	Number of stacked layers
P_i	Representative tangential force
t_i	Layer thickness
w	Sheet width
ν	Poisson's ratio of the photopolymer
ρ	Radius of curvature
ϱ	Density of the photopolymer
σ_i	Stress in layer i
κ	Bending curvature
β	Bending angle
ε_i	Strain in layer i
ε_p	Mean polymerization shrinkage of an unconstrained layer

All variables used for modeling are specified in **Table S1**.

The bending deformations of multi-layer sheets under residual stresses due to photochemical shrinkage are approximated based on multi-layer beam bending theory in a similar fashion as proposed by Timoshenko for deflections in bi-metallic strips.[S1] All stresses that act in tangential direction in each of the layers can be represented by an axial force P_i and a bending moment M_i (**Figure S1**). For consistency, all forces are assumed as tensile forces. The constitutive equations for the distinct layers are

$$M_i = \frac{E_i I_i}{\rho}. \tag{S1}$$

Equation S1 can be applied to each distinct layer of the self-bent sheets, whereby the layer moments of inertia are $I_i = \frac{w t_i^3}{12}$. The radius of curvature is equivalent to the reciprocal of the curvature $\kappa = \frac{1}{\rho}$.

After drying of the sheets, no external forces act on the bent regions of the sheets. Consequently, no net force or torque exists and the force and moment equilibria are

$$\sum_{i=1}^{n} P_i = 0, \tag{S3}$$

$$\sum_{i=1}^{n} \left\{ M_i - P_i \left(\sum_{j=1}^{i} t_j - \frac{1}{2} t_i \right) \right\} = 0. \tag{S4}$$

It is assumed that the deformations at mutual surfaces of adjacent layers are equal. Hence, a compatibility condition can be introduced based on the material behavior in each layer

$$\sigma_i = E_i \cdot \left(\varepsilon_i - \varepsilon_{p,i} \right). \tag{S5}$$

For compatibility,

$$\varepsilon_{p,i} - \varepsilon_{p,i+1} = \frac{P_i}{w t_i E_i} - \frac{P_{i+1}}{w t_{i+1} E_{i+1}} - \frac{t_i + t_{i+1}}{2\rho}. \tag{S6}$$

A closed-form solution is found by solving the system of equations (Equation S1-S6), under the assumption that the Young's Modulus in all layers is equal. The solution is

$$\rho = \frac{\left(\sum_{i=1}^{n} t_i\right)^3}{6\sum_{i=1}^{n}\sum_{j>i}^{n} t_i t_j (\varepsilon_i - \varepsilon_j)}. \quad \text{(S7)}$$

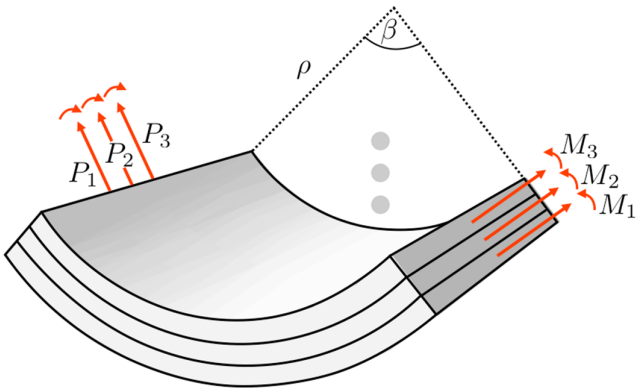

Supporting Figure S1. Mechanical model of multi-layered beam bending. A beam element is considered in a state of minimal bending stresses. All resulting forces that act in each of the layers can be represented by an axial force P_i and a bending moment M_i. The bending angle and the radius of curvature are denoted as β and ρ.

We assume that no external forces act on the sheets after deformation. The adhesion forces are assumed to act prior to delamination while the capillary action is in play only during drying. The effect of gravity is found to be negligible for the resulting bending curvature. It is evaluated by comparing the influence of gravity to the bending rigidity of the sheets. A critical length l_{crit} is introduced that defines the lateral sheet dimensions after which gravity dominates over bending rigidity and collapsing of the sheets under own weight is expected.[S2]

$$l_{crit} = \left\{\frac{E\cdot[(n-0.5)t]^2}{\varrho\cdot g}\right\}^{\frac{1}{3}} \quad \text{(S8)}$$

The critical length increases with the number of layers (**Figure S2**). Assuming a density of $\varrho = 1250\ \mathrm{kg\ m^{-3}}$ for the photopolymer,[S3] the critical length for single layer sheets is

determined as $l_{crit}(n = 1) = 2.12 \pm 0.06\,\text{mm}$. The standard deviation is determined as shown in section Data Evaluation. Since the computed critical lengths are much larger than the lateral dimensions of the sheets in use ($w = 250\,\mu\text{m}$), the effect of gravity on the bending curvature is assumed to be negligible.

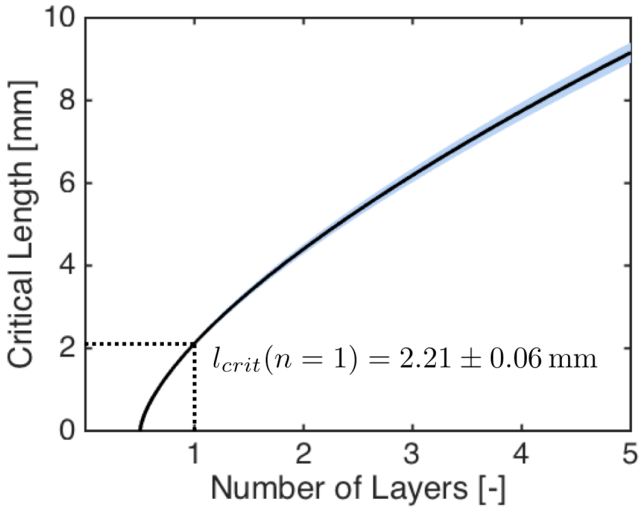

Supporting Figure S2. Influence of gravity on the self-bending curvature of laser written sheets. The shaded area indicates the standard deviation from the measurements. The critical length l_{crit} defines the lateral dimensions for which the sheets are expected to collapse under own weight.

In addition to the homogeneous in-plane shrinkage during laser writing of layers, increased deformations are observed in edge regions (**Figure S3**). Consecutive laser writing of adjacent voxel lines leads to crosslinking between the lines that reduces further shrinkage and causes residual stresses to occur in the voxel lines. Since the stresses in adjacent voxel lines are different, an in-plane bending moment is induced that causes distortions of the sheet edges. Due to the increased in-plane strains within each single layer, the induced out-of-plane bending moments in these regions is also increased. Consequently, delamination begins in the edge regions as seen in Figure 1f for sheets composed of 8-10 layers.

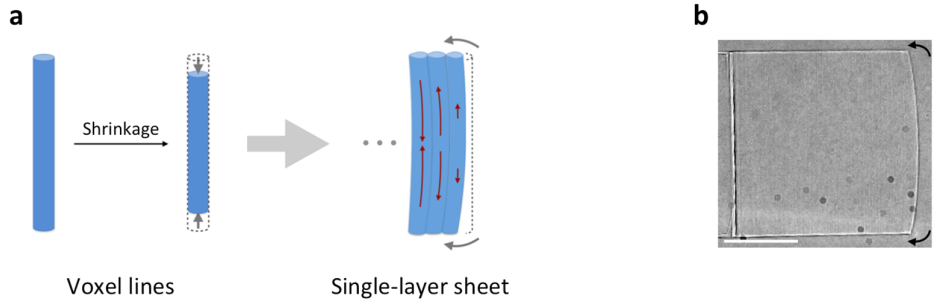

Supporting Figure S3. Edge effects during in-plane shrinkage. a) Crosslinking between adjacent voxel lines reduces shrinkage and induces residual stresses in longitudinal direction. Due to differences in magnitude and direction of the stresses, an in-plane bending moment results that leads to inward bending of the layer. b) Picture from optical microscopy of a single layer during DLW. Increased deformations can be seen in the edges on the right in the image. Scale bar: 100 µm.

Evaluation of the Young's Modulus via Nanoindentation

The investigated self-bending sheets have been fabricated from the commercially available photoresist IP-Dip (Nanoscribe GmbH, Eggenstein-Leopoldshafen, Germany). The mechanical properties of the laser written structures strongly depend on the fabrication parameters. In order to determine the Young's Modulus of the constituent bulk material we performed nanoindentation experiments. We used a 5 µm, 60° conical tip to ensure that the contact area during indentation is significantly larger than the biggest feature sizes of the fabrication process (i.e. the voxel line width). **Figure S4** shows a representative load vs. displacement curve obtained for 25 µm thick sheets. The reduced Young's Modulus was determined using the Oliver-Pharr method in the unloading cycle. The Young's Modulus of the material was approximated as

$$E = (1 - \nu^2) \cdot E_r. \quad \text{(S9)}$$

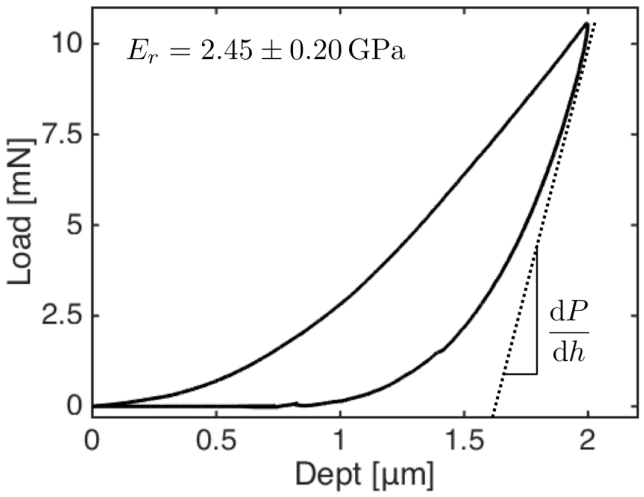

Supporting Figure S4. Representative nanoindentation measurement. From 5 independent measurements, a reduced Young's Modulus of $E_r = 2.45 \pm 0.20\,\mathrm{GPa}$ was determined for the laser written sheets. A Poisson's ratio of $\upsilon = 0.49$ was assumed for the polymerized resist.[S3]

Fabrication

With the presented method, laser writing times for 3D geometries can be drastically reduced. In DLW, laser writing in the thickness direction requires the motion of the piezoelectric scanning stage on which the substrate is mounted. Since the motion of the scanning stage is relatively slow compared to the scanning speed of the laser, the sample thickness is the main factor determining the final writing time.

For a benchmark, we compared the writing times required for the fabrication by autonomous bending of laser written 2D sheets (**Figure S5**a), and by direct 3D fabrication via DLW (Figure S5b). By fabricating the curved sample as a self-bending sheet, the writing time could be reduced by more than 70 % compared to the direct 3D fabrication.

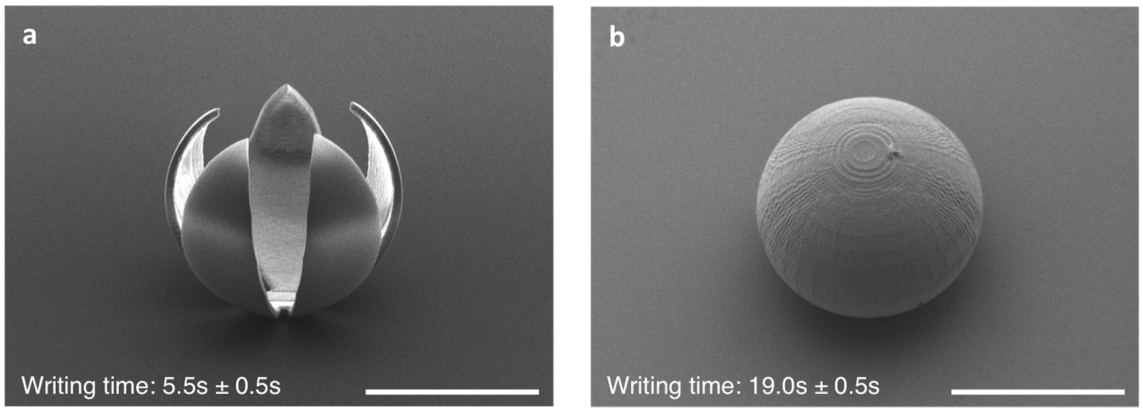

Supporting Figure S5. Writing time for a hollow spherical geometry. a) Self-bending 2D sheet that evolves into a 3D spherical geometry. b) Hollow spherical geometry that was fabricated via DLW. Scale bar: 50 μm.

We fabricated biomimetic surfaces (e.g. shark skin) with spatially controlled self-bending capability. A 2D sheet was laser written with features that autonomously bend out-of-plane upon drying (**Figure S6**a). Deforming fins were designed to bend and replicate the hydrodynamic features found in natural shark skins (Figure S6b). The presented samples were fabricated over a total surface area of 0.34 cm^2 in a single production cycle.

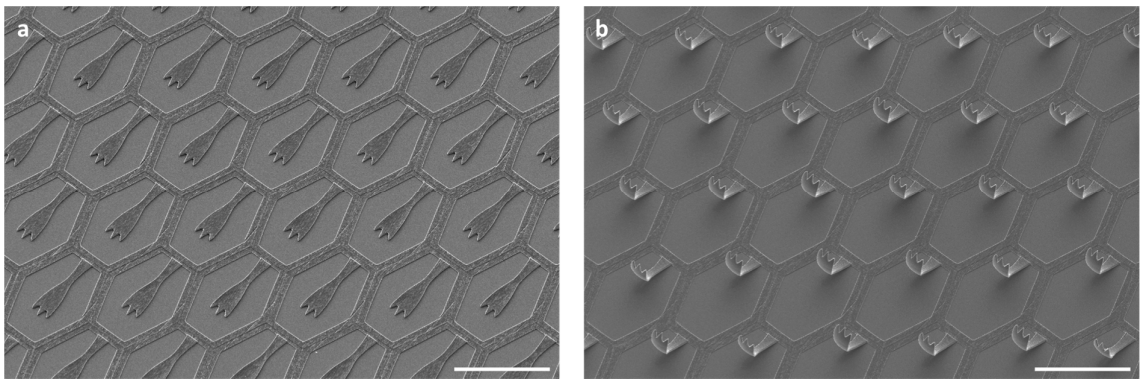

Supporting Figure S6. Biomimetic shark skin. a) Undeformed sheet. The laser written sheet comprises fins with the same dimensions found in natural shark skin and a framework that holds the fins in place. b) Controlled out-of-plane bending was achieved for sheets covering surface areas in the cm-regime. Scale bar: 250 μm.

Bending Directionality

The provided physical understanding of the bending process allows for precise control over bending curvature and directionality. The optical microscopy images in **Figure S7** show that the direction of the occurring self-bending can be controlled by changing the voxel line orientation of the sheets. Self-bending in sheets with voxel lines of 0°- and 90°-orientation is found in the direction of the voxel lines. For diagonally written sheets, boundary effects cause the corners with shorter voxel lines to detach first, resulting in bending orthogonal to the voxel line orientation. We analyzed the self-bending behavior of ~100 sheets with different voxel line orientations and found a clear correlation between voxel line orientation and bending direction.

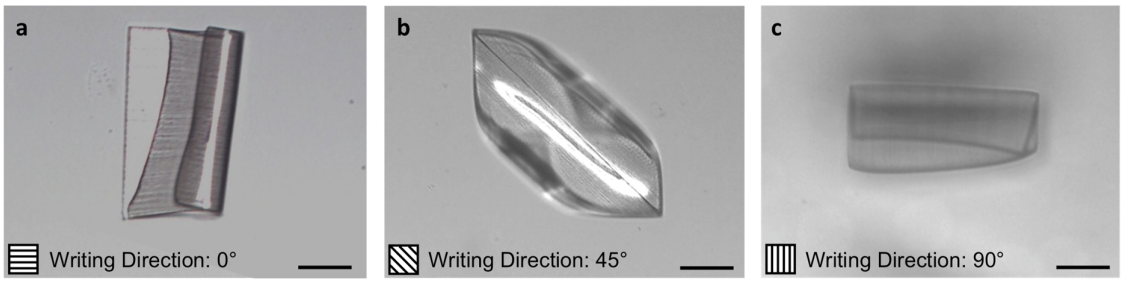

Supporting Figure S7. Optical microscopic images of laser written sheets with different voxel line orientations, resulting in different self-bending directions. Scale bars: 50 µm. a) Multi-layer self-bending sheets with voxel lines of 0°-orientation. b) Multi-layer sheets with diagonally oriented voxel lines. c) Multi-layer self-bending sheets with voxel lines of 90°-orientation.

Photochemical Shrinkage

We measured the longitudinal shrinkage of the voxel lines during photopolymerization by comparing the length of single laser written lines with two fixed ends to lines with a loose end (**Figure S8**). The polymerization shrinkage induced strain was determined as $\varepsilon_l = \frac{l-l'}{l}$, where *l* denotes the length of the voxel lines with fixed ends and *l'* that of the freely contractile lines. We computed the length of the deformed lines by summation of sections with different orientations as $l' = \sum \sqrt{{l'_x}^2 + {l'_y}^2 + {l'_z}^2}$. We also corrected for the viewing angle δ of the SEM images. By evaluating 5 samples, we found a strain of $\varepsilon_l = 16.3 \pm 1.1\%$. Only voxel lines with an approximately straight shape were evaluated. We assume that the shrinkage in the transverse direction of the voxel lines is equivalent to that in the longitudinal direction. This results in a volumetric shrinkage of $\varepsilon_v \cong 3 \cdot \varepsilon_l = 48.9 \pm 3.3\%$, which is comparable to the results reported in prior literature.[S4]

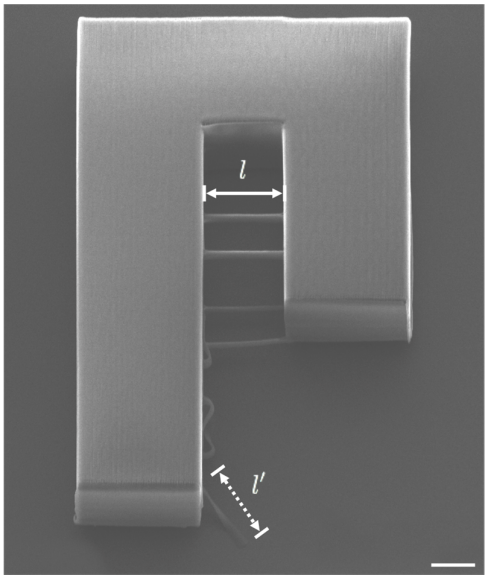

Supporting Figure S8. SEM image of a structure for measuring the longitudinal shrinkage of laser written voxel lines during polymerization. The structure consists of a geometry that holds voxel lines with two fixed endings as well as freely contractile voxel lines with a loose end. Scale bar: 10um

Voxel Line Characterization

In order to characterize the voxel size of the laser written sheets, we analyzed the edges of multi-layer sheets with SEM imaging and focused ion beam (FIB) micromachining (**Figure S9**). For the chosen DLW parameters, we found the cross section of a single voxel line to be ellipsoidal with a width of $u = 0.37 \pm 0.03$ µm and a height of $h = 2.07 \pm 0.20$ µm. Since the chosen slicing distance *t* is much smaller than the voxel height ($t \ll h$), stacking of the layers results in approximately straight columns (Figure S9a). For the modeling, we assume the bottom layer to have half the thickness of the proceeding layers $\left(t_1 = \frac{1}{2}t\right)$, accounting for the fact that it was immersed in the substrate during laser writing. We applied a focused gallium ion beam to cut a section of the corner and gain better insight into the voxel geometry (Figure S9b). The front corner of the open section reveals the ellipsoidal shape of the voxels and shows that adjacent voxel lines are connected due to double-exposure in the intervening regions (proximity effect).

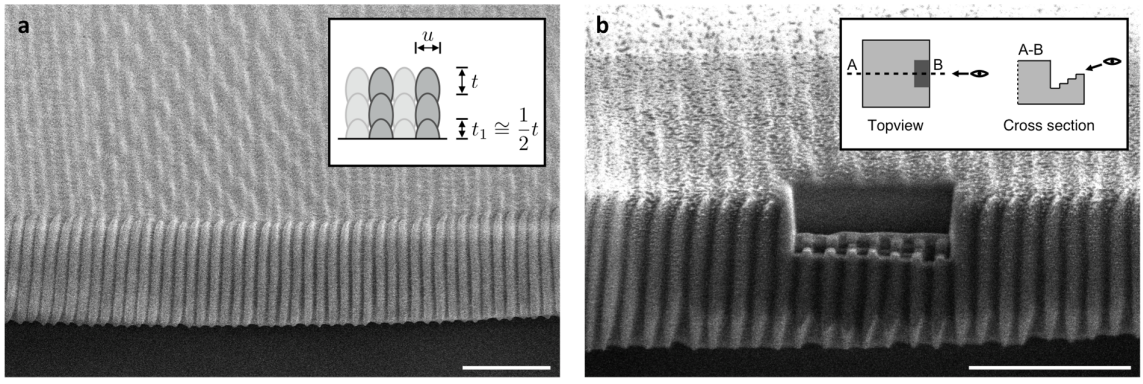

Supporting Figure S9. SEM images of parallel laser written voxel lines. Scale bars: 5um. a) Edge of multi-layer sheet. The inset depicts the cross section of stacked parallel voxel lines. b) Edge of multi-layer sheet with an open section cut out with a FIB. The inset depicts the location and geometry of the cut section.

Data Evaluation and Error Analysis

The standard deviations for all presented results were determined with the Gaussian equation for error propagation.

$$\mathrm{std}(y) = \frac{\partial y}{\partial x_1} \cdot \mathrm{std}(x_1) + \frac{\partial y}{\partial x_2} \cdot \mathrm{std}(x_2) + \cdots \quad \text{(S9)}$$

$\mathrm{std}(y)$ denotes the standard deviation of the evaluated variable, while $\mathrm{std}(x_i)$ describes the standard deviation of the measured values for the independent variable x_i.

The presented results for the reduced Young's Modulus (Figure S4) and the adhesive tension (Figure 2c) have been computed from 5 consecutive measurements on separate samples, respectively. The values for the polymerization shrinkage ε_p and the bending angles (Figure 2f) have been acquired from 10 consecutive measurements on separate samples, respectively.

References

[S1] S. Timoshenko, *J. Opt. Soc. Am.* **1925**, *11*, 233.

[S2] B. Roman, J. Bico, *J. Phys. Condens. Matter* **2010**, *22*, 493101.

[S3] E. D. Lemma, F. Rizzi, T. Dattoma, B. Spagnolo, L. Sileo, A. Qualtieri, M. De Vittorio, F. Pisanello, *IEEE Trans. Nanotechnol*. **2017**, *16*, 23.

[S4] K. Takada, D. Wu, Q.-D. Chen, S. Shoji, H. Xia, S. Kawata, H.-B. Sun, *Opt. Lett.* **2009**, *34*, 566.